Effects of Injection Pressure Variation on Mixing in a Cold Supersonic Combustor with Kerosene Fuel

Wei-Lai Liu[1], Lin Zhu[2*], Yin-Yin Qi[2], Jia-Ru Ge[2], Feng Luo[2], Hao-Ran Zou[2], Ming Wei[2], Tien-Chien Jen[3]

1. Department of Precision Machinery & Precision Instrumentation, University of Science & Technology of China, Hefei, 230027, China

2. Lab of Mechanical Structure & Biomechanics, Anhui Agricultural University, Hefei, 230036, China

3. Mechanical Engineering Department, University of Johannesburg, Johannesburg, 2006, South Africa

Abstract

Spray jet in cold kerosene-fueled supersonic flow has been characterized under different injection pressures to assess the effects of the pressure variation on the mixing between incident shock wave and transverse cavity injection. Based on the real scramjet combustor, a detailed computational fluid dynamics model is developed. The injection pressures are specified as 0.5, 1.0, 2.0, 3.0 and 4.0 MPa, respectively, with the other constant operation parameters (such as the injection diameter, angle and velocity). A three dimensional Couple Level Set & Volume of Fluids approach incorporating an improved Kelvin-Helmholtz & Rayleigh-Taylor model is used to investigate the interaction between kerosene and supersonic air. The numerical simulations primarily concentrate on penetration depth, span expansion area, angle of shock wave and sauter mean diameter distribution of the kerosene droplets with/without evaporation. Validation has been implemented by comparing the calculated against the measured in literature with good qualitative agreement. Results show that the penetration depth, span-wise angle and expansion area of the transverse cavity jet are all increased with the injection pressure. However, when the injection pressure is further increased, the value in either penetration depth or expansion area increases appreciably. This study demonstrates the feasibility and effectiveness of the combination of Couple Level Set & Volume of Fluids approach and an improved Kelvin-Helmholtz & Rayleigh-Taylor model, in turn providing insights into scramjet design improvement.

Key words: Injection pressure, Transversal cavity injection, Cold supersonic flow, Couple Level Set & Volume of Fluids (CLSVOF), Improved Kelvin-Helmholtz (K-H) & Rayleigh-Taylor (R-T) model

1. Introduction

The jet-in-crossflow process is of particular importance in hypersonic vehicles because of its operations at high Mach number, e.g. at Mach 8. Sufficiently high speed generally leads to significantly short residence time of the free-stream within the combustion chamber, which in turn incurs incomplete mixing and strongly affects the combustion efficiencies [1]. Therefore, the study of the flow topology related to the liquid jet injecting into supersonic flow is intriguing and meaningful. Current design of the optimum injection system with great performance capabilities is really a challenge [2]. In this regard, the fundamental mechanism of the liquid jet in the high speed crossflows must be understood.

Currently, studies have already focused on the design of injector systems for improving the fuel-air mixing characteristics. For example, transversal fuel injection through a wall orifice is considered to be one of the simplest and most conventional approaches for the scramjet engine, possibly due to its better fuel penetration, interaction, and mixing [3-6]. Abdelhafz et al. [7] numerically investigated oblique and transverse configurations as gaseous fuel was injected into a low-aspect-ratio supersonic combustor. They claimed that injecting fuel obliquely can result in higher mixing efficiencies. Huang et al [8] addressed the effect of injection angle of helium, under various pressure conditions, on the interaction between fuel and incoming air in the transversal injection flow field. They concluded that Re-normalization group (RNG) $k-\varepsilon$ turbulence model is better in predicting the wall pressures under low jet-to-crossflow pressure ratios, whilst shear stress transport (SST) $k-\varepsilon$ is more appropriate for high jet-to-crossflow pressure ratios. Hu et al. [9] studied the performance of a scramjet combustor with kerosene fuel injected from a strut

under different equivalence ratios and observed that the mixing characteristics greatly vary with the strut fuel feeding ratio, especially when this ratio is close to the lowest and the highest limits. However, to the authors' knowledge, there are few studies in literature for the injection-pressure effects on fuel-air mixing characteristics in a cold kerosene-fueled supersonic air-stream. This emphasis is on the mixing characteristics in the kerosene-fueled supersonic flow field, and especially on the effects of the injection pressure on the interaction between incident shock wave and transversal cavity injection.

2. CFD Model and Simulation Approach

2.1. Model geometry

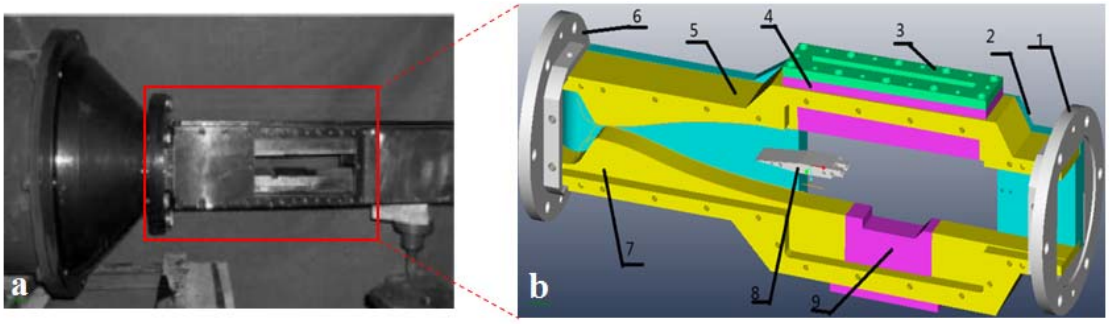

Fig.1. (a) A real prototype and (b) A 3D model of the scramjet combustor: 1. flange, 2. rear cover, 3. pressure pad of upper glass window, 4. upper glass window, 5. upper cover, 6. flange, 7. lower cover, 8. strut, 9.cavity

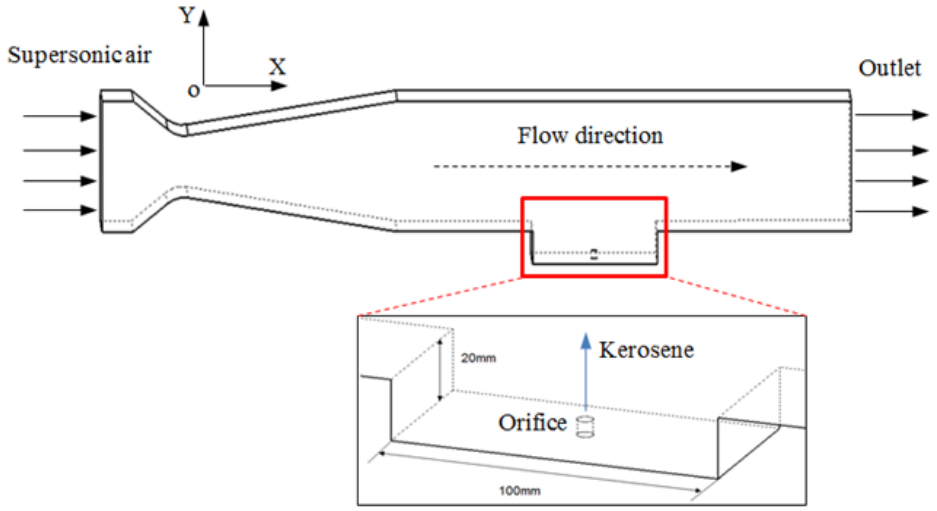

Fig.2. Schematic of the scramjet combustor geometry

Figure 1 shows the real prototype and the corresponding three-dimensional (3D) model of the scramjet combustor developed by Liu [10]. The real scramjet combustor contains flange 1 and 6, pressure pad of upper glass window 3 and upper glass window 4. However, to simply the CFD model in this study, we have ignored the above-mentioned components due to no effects on the kerosene-air interaction and due to the reduced calculation time. Meanwhile, although strut 8 affects the flow behavior of the mixture in the combustor, it is not considered either because no related component exits in the present experimental setup of Liu's. Thus, the scramjet combustor herein only consists of rear cover 2, upper cover 5, lower cover 7 and cavity 9. Figure 2 shows the simplified 3D geometry of the scramjet combustor by using feature-based modeling [11]. Table 1 shows the primary specifications of the combustor for calculations. Note that the incident shock wave generated by kerosene is injected from the orifice at

the center of the cavity, as shown in Fig.2.

Table 1

Specifications of the scramjet combustor

Item	Dimension
Scramjet combustor	$0.6\times0.05\times0.08m^3$ (length × width × height)
Cavity	$0.1\times0.05\times0.02m^3$ (length × width × height)
Orifice	$1.0\times10^{-3}m(\Phi)$,0.02m long
Inlet & outlet	$0.05\times0.08m^2$ (width × height)

2.2. CFD modeling

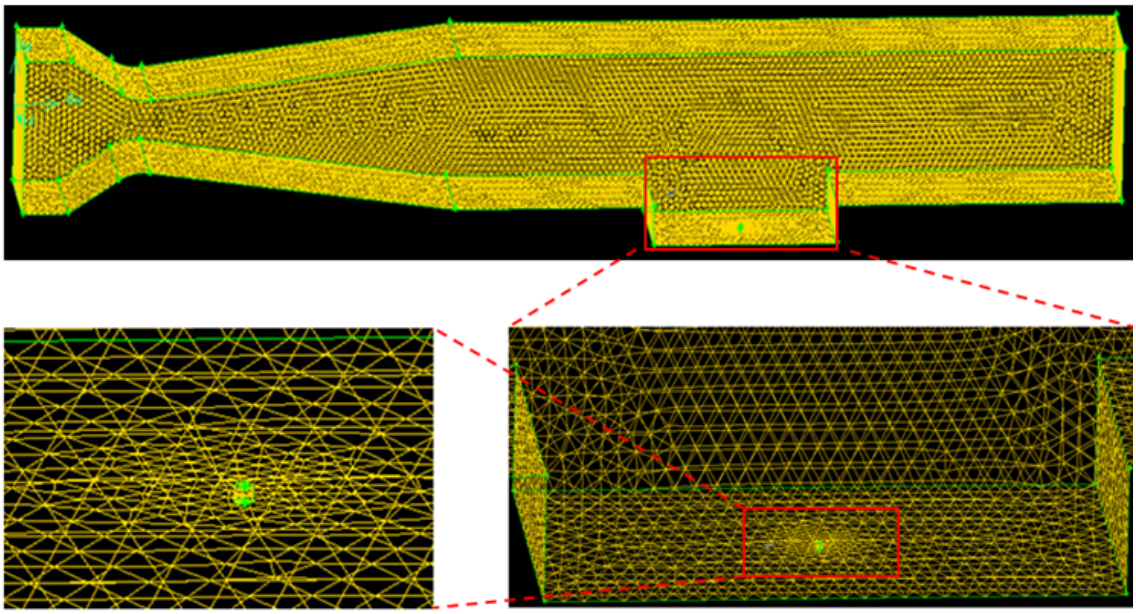

Fig.3. Details of numerical grid of the scramjet combustor

The meshed CFD model of the scramjet combustor is shown in Fig.3, where the total of 330,000 hexahedron cells is used. As observed, the mesh cells are concentrated around either the walls or the region near the cavity due to the strong interaction between incident shock wave and transverse cavity injection.

Currently, the supersonic air-fuel interaction is predicted by using commercial CFD software ANSYS Fluent 14.0, in which volume of fluids (VOF) model is generally used to calculate the interface breakup and coalesce with another interface [12]. But, when a large deformation of the gas-liquid interface is involved additional re-meshing is greatly necessitated [13]. The mixing process of incident shock wave and transverse cavity injection in supersonic flows facilitates the more complex turbulent structures. Hence, in this study three dimensional Couple Level Set & Volume of Fluids (CLSVOF) model is proposed to investigate the effects of the injection pressure on the mixing characteristics between supersonic flow and kerosene in the cold scramjet combustor. This may be explained as due to the fact that the CLSVOF model, coupling the LS (Level Set) and VOF, not only contains their common advantages but also overcomes their disadvantages [14]. For CLSVOF, a single set of the conservation equation is used for the whole domain and there are no separate gas-liquid velocities. Consequently, the Navier-Stokes has the following form [14]:

$$\int_v \frac{\partial(\rho u)}{\partial t} + \int_v \nabla g(\rho u \otimes u) = -\int_v \nabla p + \int_v \nabla g(2\mu D) + \int_v F_{st} + \int_v \rho g \tag{1}$$

and the continuity equation is

$$\int_v \frac{\partial \rho}{\partial t} + \int_v \nabla g(\rho u) = 0 \tag{2}$$

where $\vec{V}$ is a velocity vector, ρ—fluid density, t—time, μ—fluid viscosity, D—viscous deformation tensor, g—gravity vector and F_{st}—body force due to the surface tension.

In addition, such the other governing equations as the energy equation, the state equation of gaseous mixture and the turbulent model are also taken into account in this study. The detailed formulas are presented below, respectively.

The energy equation for a droplet is [15]:

$$\mathrm{m}\frac{de}{dt} = q + Q_s, \text{ where } e = c_{vs}T_s + h_f^0, \quad Q_s = \frac{dm}{dt}h_L \tag{3}$$

where Q_s is the energy of phase transitions, the heat flux q to a single droplet from the surrounding gas flow is determined by [16]

$$q = \begin{cases} \pi d\lambda \cdot Nu \cdot (T - T_s) & \mathrm{Re} < 1000 \\ \pi d^2 \rho \left|\vec{v} - \vec{u}\right| \cdot St \cdot (H_r - H_w) & \mathrm{Re} \geq 1000 \end{cases} \tag{4}$$

where $Nu = 2 + 0.16 \cdot \mathrm{Re}^{2/3} \cdot \mathrm{Pr}^{1/3}, St = \frac{C_d}{2}\mathrm{Pr}^{-2/3}$, $\vec{v}$—droplet velocity, $\vec{u}$—fluid velocity, T—gas temperature, T_s—droplet temperature.

The state equations for the gaseous mixture are [17]:

$$P = R_g \rho T \sum_k Y_k / W_k$$

$$E = \sum_k Y_k (c_{vk} T + h_{ok}) + \frac{\vec{u}^2}{2} + k \tag{5}$$

where E is the gas energy, P—the gas pressure, k—the turbulent kinetic energy, W_k—the molar mass of the kth gas component, h_{ok}—the specific chemical energy, c_{vk}—the specific heat capacity, Y_k—the mass concentration of the kth gas component, R_g—the universal gas constant.

The turbulent model is presented as follows [18]: the two-equation shear stress transport (SST) model developed by Menter is used for the turbulence in the cold supersonic flow because of its combined advantages of both k-ω model and the k-ε model. The SST turbulence model consists of two equations: one for k, the specific turbulent kinetic energy ($m^2\ s^{-2}$) (Eq.6) and the other for ω, the specific turbulence dissipation rate (or specific turbulent frequency) (s^{-1}) (Eq.7). Eq. 8 shows the formula on the turbulent viscosity.

$$\frac{\partial}{\partial t}(\rho k)+\frac{\partial(\rho u_j k)}{\partial x_j}=\rho P-\beta^*\rho k\omega+\frac{\partial}{\partial x_j}[(\mu+\sigma_k\mu_t)\frac{\partial k}{\partial x_j}] \tag{6}$$

$$\frac{\partial}{\partial t}(\rho\omega)+\frac{\partial}{\partial x_j}(\rho u_j\omega)=\frac{\gamma}{\nu_t}P-\rho\beta\omega^2+\frac{\partial}{\partial x_j}[(\mu+\sigma_\omega\mu_t)\frac{\partial\omega}{\partial x_j}]+2(1-F_1)\frac{\rho\sigma_{\omega 2}}{\omega}\frac{\partial k}{\partial x_j}\frac{\partial\omega}{\partial x_j} \tag{7}$$

where $P=\tau_{ij}\dfrac{\partial u_i}{\partial x_j}$, $\sigma_i(i=k,\omega)$—diffusion constants of the model. We refer the readers to the work of Menter [18] for details of the equations.

All the simulations in this paper are implemented with an implicit CFD code. This code solves the governing equations, i.e. Reynolds averaged Navier-Stokes (RANS) equations using cell centered finite volume approach. A second order upwind scheme is employed to discretize both momentum and continuity equations with a coupled solver, i.e. the pressure-based (coupled) double precision solver. The convective fluxes are treated using the Roe Flux-Difference Splitting Scheme, which has been demonstrated to have the potential for improving treatment and accuracy at shock [19].

The boundary conditions for the CFD modeling are specified to mostly match the experimental scenarios supplied by Liu. This purpose is that the numerical simulations will be compared against further measurements. Note that due to the ignored flange uniformly distributed speed, pressure and temperature are assumed on the air inlet.

The coming air is assumed to be a thermally and calorically perfect gas and the mass-weighted-mixing law of viscosity is utilized. The key operation properties of the supersonic flow are specified as a Mach number of 2.2 and a stagnation pressure P_0 of 7.85 MPa. For the kerosene jet, the operational parameters are set to be an injection velocity of 70 ms^{-1}, an injection diameter of 1.0 mm and injection pressures of 0.5, 1.0, 2.0, 3.0, and 4.0 MPa. The other parameters of kerosene, e.g. density, viscosity and surface tension are kept constant at ρ=0.78 g/cm^3, u=2 mPas and σ=23.6×10^{-3} N/m, respectively.

A fixed pressure of 1.013×10^5 Pa is specified at the inlet and outlet of the scramjet combustor, respectively. No-slip boundary conditions are used for the channel wall, where the standard wall functions defined in FLUENT are applied to model the near-wall region flow. The stagnation temperature T_0 is designated as 300K. In addition, following the turbulence model used in this study, i.e. the Menter's two-equation shear stress transport (SST) k-ω model, the turbulence characteristic values are specified as follows: turbulence intensity—8%, hydraulic diameter—1.0 mm, and the courant-Friedrichs-Levy (CFL) number also remains at 0.5 with suitable under-relaxation factors to ensure stability.

3. Results and Discussion

3.1. Numerical accuracy

For a more accurate numerical result, two key factors are generally addressed. One is grid scale and the other is convergence and discretization error. The current study on grid-dependency has demonstrated that for supersonic flow the grid scale has slightly influences on the transverse injection flow field [20]. For this reason, we select the medium size of the grid for all simulations in order to save the calculation time. Such the grid treatment (330,000 hexahedron cells), as shown in section 2.2, is believed to guarantee the high level of accuracy.

The method of convergence and discretization error analysis is based on the previous numerical investigations, where the computational model is considered to be in convergence if the residuals of the flow field parameters, e.g. continuity and momentum etc. all fall below a certain order of magnitude [21]. To achieve the solution convergence of the steady state, we optimize both courant-friedrichs-levy (CFL) number and under-relaxation factors. The solution

convergence is judged in accordance with the residuals of the governing equations. In detail, all the calculations are stopped and remain stable as the residual of each equation is smaller than 1.0×10^{-3}. The average time step is designated as 10 μs, and a typical run actually takes 2127 time steps to a real time of about 22 ms. Figure 4 shows the residual evolutions of the different flow field parameters vs the iteration number for the different injection pressures. These operation parameters include continuity, velocity, energy, k and omega. As shown in Fig.4, the iteration number for the injection pressures of 0.5, 1.0, 2.0, 3.0 and 4.0 MPa approximates 400 as the computational model of the scramjet is in convergence. Note that the situation that all but energy is less than a certain value, e.g. 10^{-3} is also considered to be converged [21].

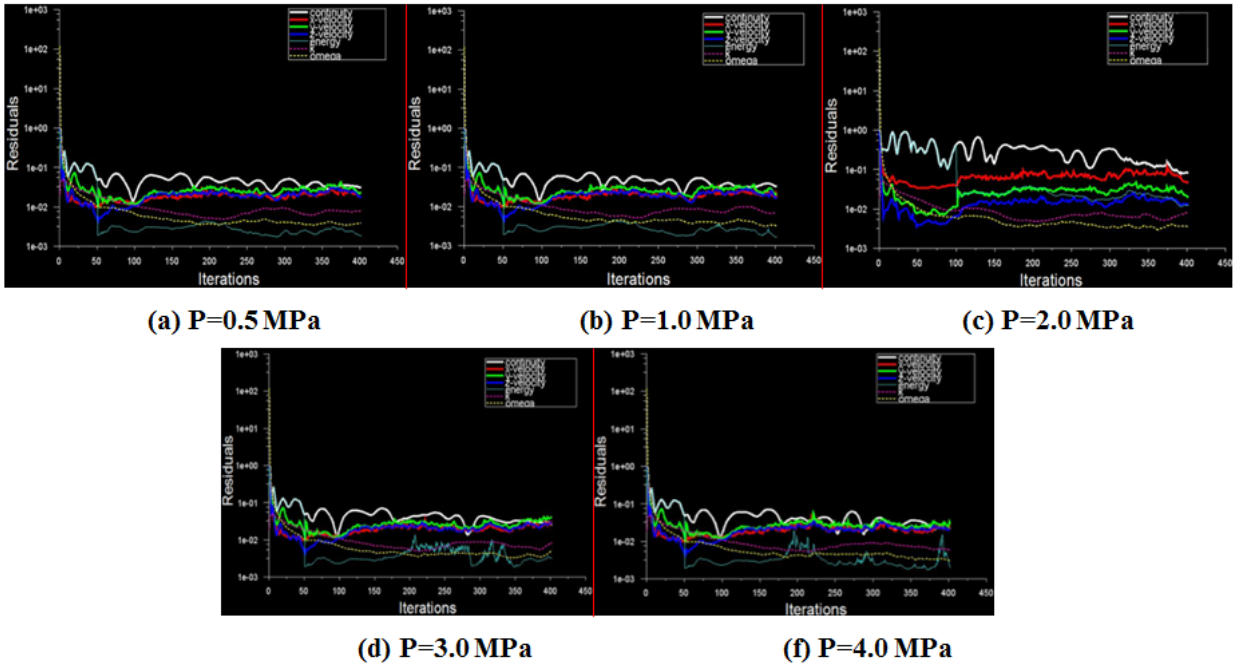

Fig.4. Residual variation with iteration number under the different injection pressures

3.2. Penetration depth

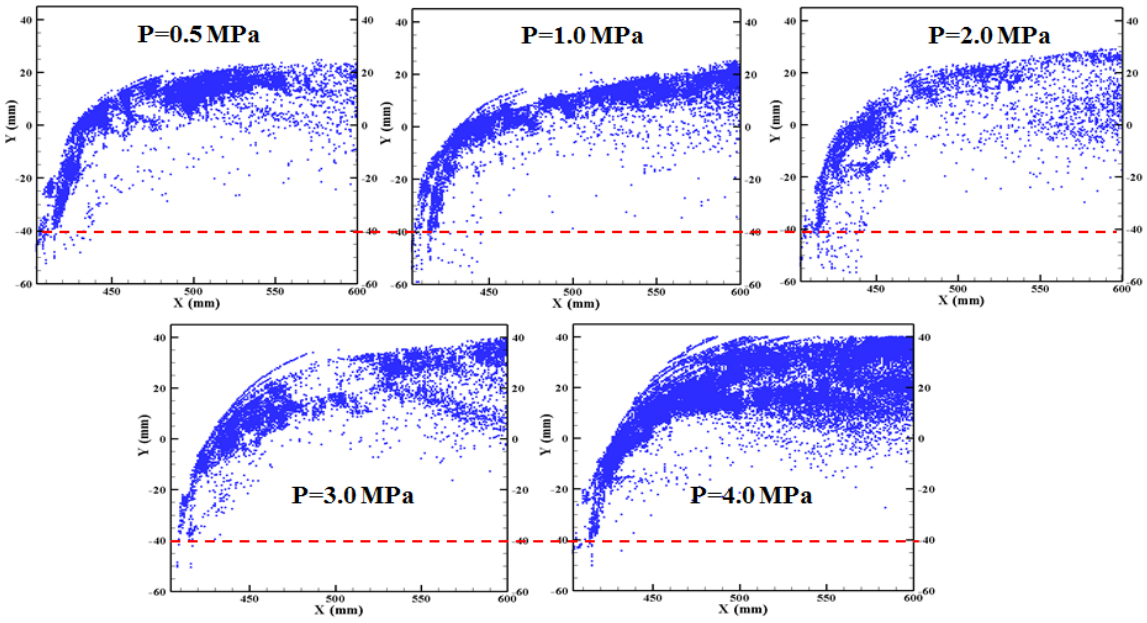

Fig.5. Penetration depths of the kerosene jet under the different injection pressures

Figure 5 shows the penetration depths of the kerosene jet for five different injection pressures. As observed, all

the flow structures consist of such similar primary compression shock, compression shock normal to the wall and curved central compression shock with [22]. For the baseline of y= −40 mm (the red dashed line in Fig.5), most of the kerosene droplets approximately appear in the range of -40 to 20 mm,−40 to 25 mm,−40 to 30 mm,−40 to 39 mm, and −40 to 40 mm, corresponding to the different injection pressures of 0.5, 1.0, 2.0, 3.0, and 4.0 MPa. Hence, it is inferred that at the identified injection velocity, angle and diameter, the penetration depth of the kerosene droplets increases with the injection pressure. This can be explained as follows: an increase in injection pressure of the liquid jet from the orifice contributes to an increase in total momentum and hence in inertia force. Consequently, the increased inertia force causes the liquid jet to deflect difficultly, thereby enlarging the penetration depth.

Figure 5 also shows that the penetration depth increases appreciably as the injection pressure is further increased. For example, for the two different injection pressures of 3.0 and 4.0 MPa, the difference in penetration depth is very little. This may be due to the nonlinear relationship between the injection velocity and the spray pressure and due to the enhanced effect of the total momentum of the supersonic air on the liquid jet. Hence, we conclude that even if the injection pressure can provide some increase in the penetration depth, its effect in the practical applications is shown to be less pronounced than anticipated.

3.3. Span expansion area

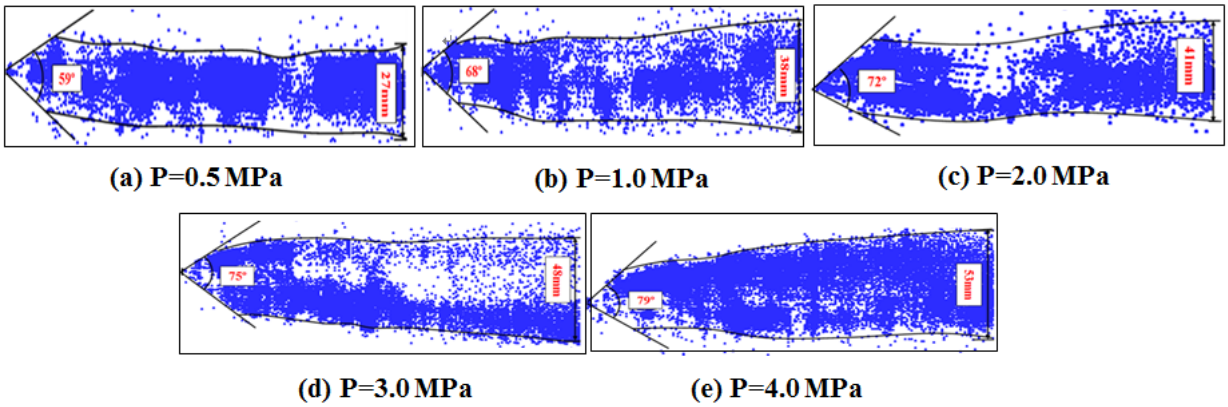

Fig.6. Span-wise expansion area of the kerosene jet under the different injection pressures

Figure 6 shows the span expansion variations of the kerosene jet at five different injection pressures of 0.5, 1.0, 2.0, 3.0, and 4.0 MPa. Note that this expansion area is obtained on the plane XOZ, which is 60 mm vertically away from the orifice in the cavity (Fig.2). As observed, the span area of the kerosene jet is increased with the injection pressure. In detail, the expansion breadths and angles of the kerosene jet approximately increase from (27 mm, 59^0) to (38 mm, 68^0), (41 mm, 72^0), (48 mm, 75^0), and (53 mm, 79^0), respectively. This variation can be explained as due to the fact that the increased injection pressure leads to the increased momentum of the kerosene jet. The greater momentum contributes to the more injection mass and the higher injection speed of the kerosene jet and hence enlarges the expansion area.

3.4. Angle of shock wave

Figure 7 shows the angle of shock wave of the kerosene jet at five different injection pressures of 0.5, 1.0, 2.0, 3.0, and 4.0 MPa. From Fig.7, it can be seen that the predicted shock wave angle is increased with the injection pressure. In the range of injection pressure of 0.5 to 4.0 MPa, the shock wave angle increases from 58º to 61º, 65º, 70º, and 72º,respectively, and that the injection distance of the kerosene droplets, at the outlet of the combustor in Fig.2, is also increased from 23 mm to 25 mm, 29 mm, 39 mm, and 40 mm, respectively. These numerical predictions are in qualitative agreement with those in Fig. 5. Hence, it is clearly concluded that under the effect of the injection

pressure the kerosene droplets are inclined to mixing with the incoming flow and atomization due to the shock wave angle. This increase can be explained by the increase in the initial momentum of the liquid jet due to the increased injection pressure. In detail, the increase in momentum trends to enhance the flow rate of the liquid jet and hence the penetration depths; the larger penetration depth indicates the stronger compression effects of the liquid jets on the incoming flow, which subsequently enlarges the angle of shock wave. However, it should be noted that further increasing the injection pressure seems to have appreciable effect on the shock wave angle (see the cases of 3.0 and 4.0 MPa in Fig.7). This may be attributed to the relatively slow increase rate of the penetration depth as shown in Fig.5.

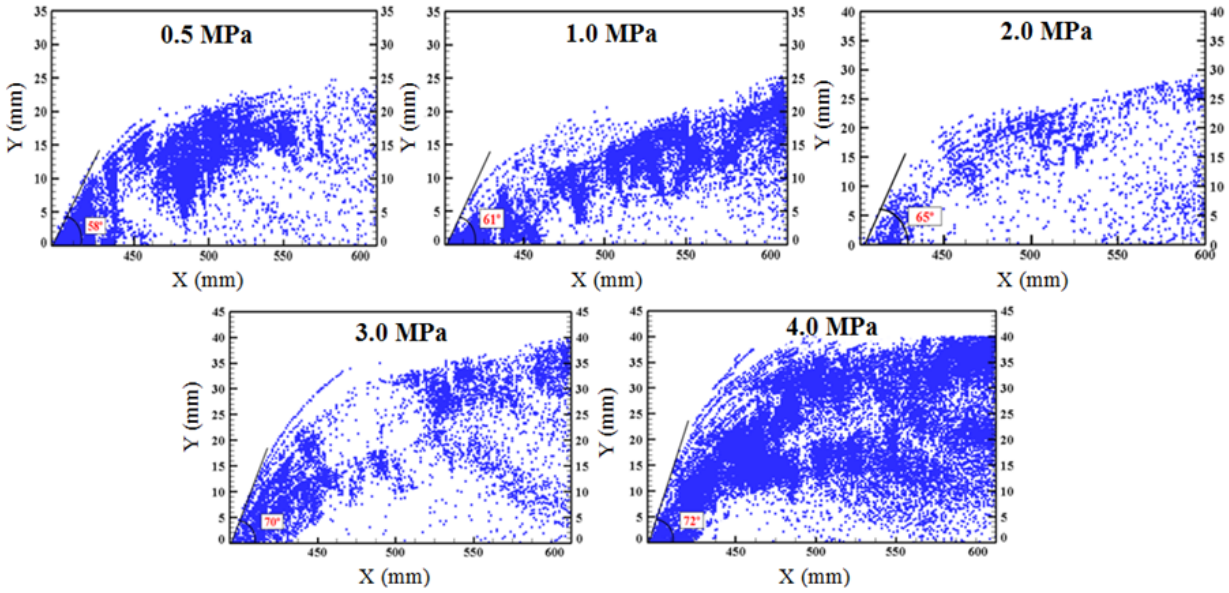

Fig.7. Angle of the shock wave of the kerosene jet under the different injection pressures

3.5. Sauter mean diameter (SMD) distribution

To achieve the droplet atomization, we have used a combination of a Blob model and an improved Kelvin-Helmholtz (K-H) & Rayleigh-Taylor (R-T) model for SMD distributions. In detail, for simplicity, the Bob model is employed for the primary atomization, in which the droplet size is equal to the injection diameter, i.e. 1.0 mm in this study, whilst the improved K-H & R-T model, i.e. K-H & R-T model II is used for the investigation of the droplet's breakup because this model has been successfully used at the similar settings in supersonic flow [23-24]. The detailed description on the K-H & R-T model II is presented as follows [23]: as the liquid jet injects from the orifice a shear interaction occurs between the liquid jet and the supersonic flow, when a K-H wave appears around the liquid jet and results in so many droplets peeling off the liquid jet; the K-H model is most appropriate for this process. As the liquid jet enters into the combustion chamber, the droplets continuously peel off the liquid jet and simultaneously the peeled droplets begin to break up. At this point, it is so reasonable to consider the foregoing phenomenon by using a combination of K-T wave and R-T wave. Consequently a combined K-H & R-T model is better to characterize this process. Note that there is a key to address, namely the time when the R-T model is incorporated into the K-H model to simulate the droplets' atomization. The related formulas for the SMD distributions are briefly presented as follows [23].

1) K-H model

$$\frac{\Lambda}{r} = 9.02\frac{(1+0.45Oh^{0.5})(1+0.4T^{0.7})}{(1+0.87We_g^{1.67})^{0.6}} \tag{9}$$

$$\Omega\left[\frac{\rho_d r^3}{\sigma}\right]^{0.5}=\frac{0.34+0.38We_g^{1.5}}{(1+Oh)(1+1.4T^{0.6})} \tag{10}$$

where Λ is the surface wave length of the liquid jet at the maximum growth rate Ω, $Oh=\sqrt{We_d}/\mathrm{Re}_d$ —Ohnesorge number of the droplets, $T=\sqrt{We_d}Oh$, $We_d=\rho_d r v^2/\sigma$ —Weber number of the droplet, ρ_d —the density of the liquid jet, σ is the surface tension at the interface , We_g —Weber number of the gas, and r—the radius of the droplet.

The mean radius r*of the droplets after breakup is

$$\mathrm{r}^*=\begin{cases} B_0\Lambda & B_0\Lambda\le r \\ \min\begin{cases}(3\pi r^2 v/2\Omega)^{0.33} \\ (3r^2\Lambda/4)^{0.33}\end{cases} & B_0\Lambda>r\end{cases} \tag{11}$$

The breakup velocity of the droplets is

$$\frac{dr}{dt}=-\frac{(r-r^*)}{\tau_b} \tag{12}$$

where $\tau_b=3.726B_1 r/\Lambda\Omega$; $B_0=1.22$, $B_1=30$.

2) R-T model

$$\Omega_{RT}=\sqrt{\frac{2}{3\sqrt{3\sigma}}\frac{[-g_d(\rho_d-\rho_g)]^{3/2}}{\rho_d+\rho_g}} \tag{13}$$

where Ω_{RT} is the frequency of the unsteady wave at the maximum growth rate, g_d — the acceleration of the droplets

The breakup time τ_{RT} for the droplets is

$$\tau_{RT}=\frac{C_\tau}{\Omega_{RT}} \tag{14}$$

The mean radius r* of the droplets after breakup is

$$r^*=\frac{\pi C_{RT}}{K_{RT}} \tag{15}$$

Where $C_\tau=1, C_{RT}=0.35$, and K_{RT} is a wave number determined by

$$K_{RT}=\sqrt{\frac{-g_d(\rho_d-\rho_g)}{3\sigma}} \tag{16}$$

3) The time criterion on incorporating R-T model into K-H model

As depicted above, the liquid jet enters into the combustion chamber, where the droplets continuously peel off the liquid jet and simultaneously the peeled droplets begin to break up. The aforementioned process is affected by both the K-H wave and the R-T wave. At this point the time criterion on incorporating the R-T model into the K-H model can be determined by Eq. (17) [23]. It should be noted that for Eq. (17) if $t<t_b$, the breakup of the droplets is simply calculated by using the K-H model, whilst if $t\ge t_b$, it is simulated by using a combination of K-H and R-T models.

$$\left.\begin{array}{c} t_b / t^* = 5.0 \\ t^* = d_d \sqrt{(\rho_d / \rho_g)} / v \end{array}\right\} \tag{17}$$

where t_b is the breakup time of the droplets, t^* —the characteristic time, and d_d —the diameter of the droplet.

In addition, in order to further evaluate the mixture quality, we have also taken into account the evaporation of the kerosene droplets in all simulations. Due to the non-uniformity interaction between fuel and air in supersonic cross flow, the non-equilibrium evaporation model is utilized to determine the evaporation rate [25-26]

$$\dot{m} = \pi d \cdot \rho_g D \cdot N\mu \cdot \log(1 - Y_e / 1 - Y_w) \tag{18}$$

$$Y_w = \frac{W_N P_0}{W_p} \exp[\frac{H_b}{R}(\frac{1}{T_b(P_0)} - \frac{1}{T_s})] - \dot{m}\frac{\sqrt{2\pi R T_s}}{\pi \delta_e p d^2} \tag{19}$$

where d is the diameter of the droplet, ρ_g —the density of the gas, D—mass diffusion coefficient, and $N\mu$ —Nusselt number of the mass transfer.

The related thermal characteristics of gas and droplet for evaporation are specified as follows: ambient pressure $p=1.013\times10^5$ Pa, initial droplet temperature—T=300K, static temperature of the gas (considering evaporation) —T=536K, gaseous phase—air, liquid—kerosene, mass diffusivity (m^2/s) —2.88×10^{-5}, thermal conductivity (W/m·k) —0.0454, and the latent heat h_L of evaporation—226kj/kg.

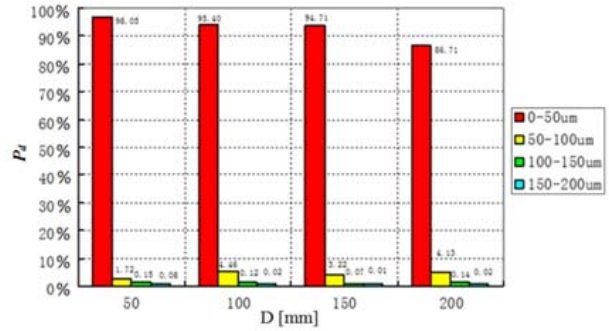

(a) P=0.5MPa

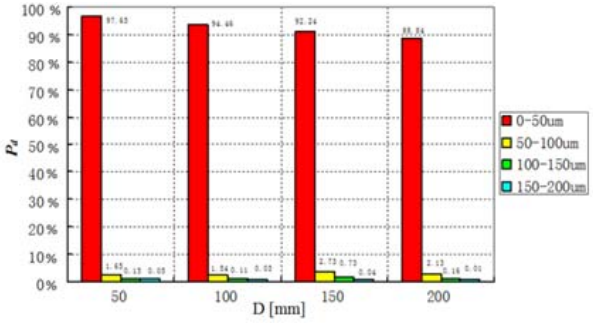

(a) P=0.5MPa

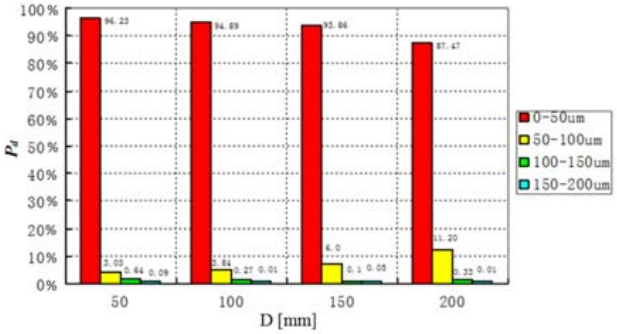

(b) P=1.0MPa

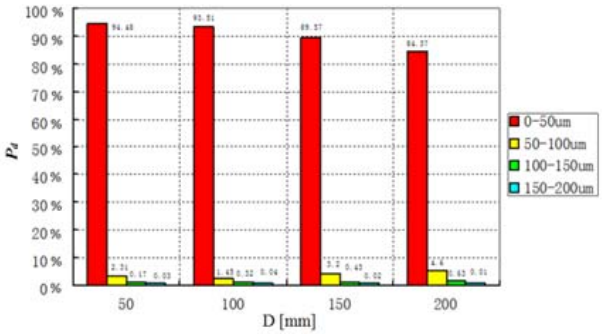

(b) P=1.0MPa

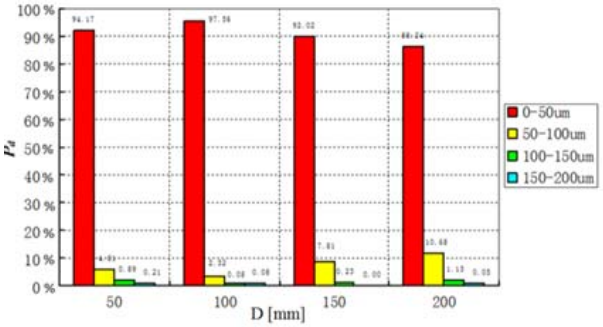

(c) P=2.0MPa

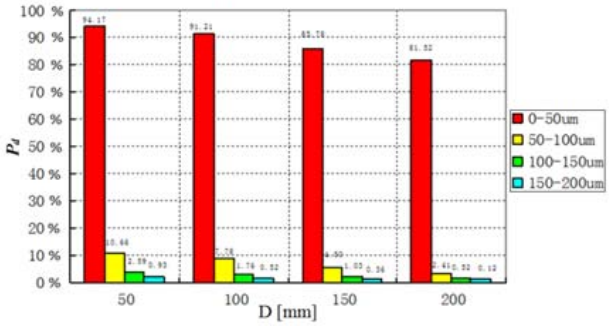

(c) P=2.0MPa

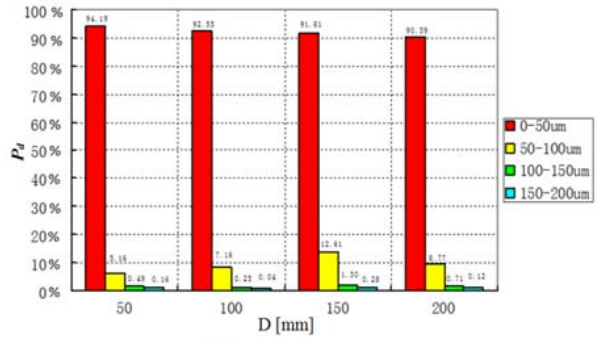

(d) P=3.0MPa

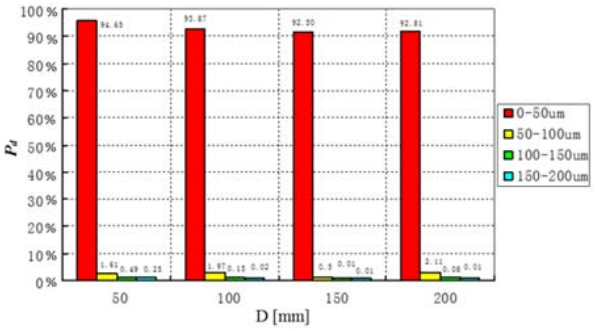

(e) P=4.0MPa

Fig.8. SMD distribution of the kerosene droplets under the different injection pressures without any evaporation

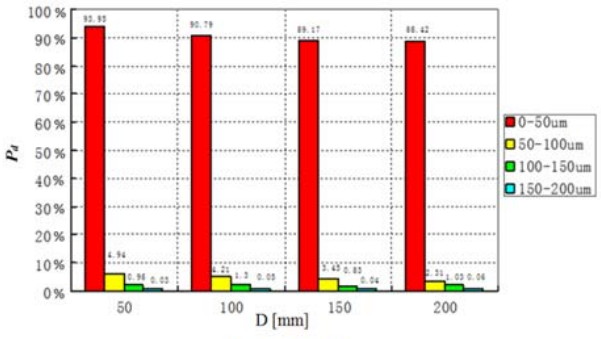

(d) P=3.0MPa

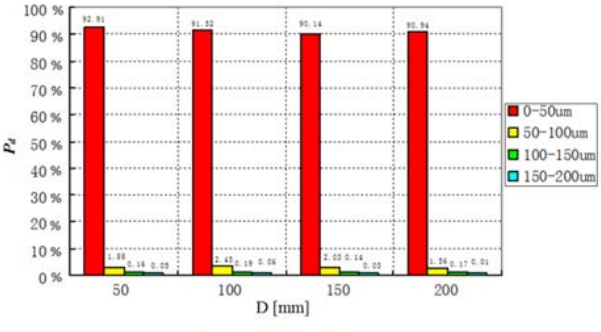

(e) P=4.0MPa

Fig.9. SMD distribution of the kerosene droplets under the different injection pressures with any evaporation

Figures 8~9 show the sauter mean diameter (SMD) distributions of the kerosene droplets along the x direction without/with the kerosene evaporation considered. These numerical simulations are obtained for the injection pressures in the range of 0.5 to 4.0 MPa. Note that in both pictures P_d indicates the percentage of the SMD distribution of droplets at the cross-section vertical to the supersonic flow direction and D denotes the distance between the cross-section and the orifice in the cavity.

Without the evaporation, as shown in Fig.8, the concentration of the kerosene droplets varies along the x direction as the injection pressure is increased from 0.5 to 4.0 MPa. One interesting finding is that at the location about 50mm away from the orifice the greatest number of the smallest droplets (0~50 um), namely 98.05% of the droplets, appears in the case of 0.5 MPa and that when the injection pressure is increased to 4.0 MPa, the greatest number of the smallest droplets, about 92.81%, is located at the outlet of the combustor. Note that 98.05% and 92.81% presented here are both accounted for the smallest droplets of all kerosene jets in this study. It is thus concluded that for no evaporation, the number of the smallest kerosene droplet is dependent on the injection pressure. For the greatest number of the smallest droplets at 0.5 MPa, this may be explained as due to so low penetration height at the cavity, which causes so many droplets to meet with the air and subsequently have the strongest shear interaction with each other; while for the scenario at 4.0 MPa, it may be attributed to the increased momentum of the liquid jet with the injection pressure, which uplifts the penetration height of the droplets and thus increases the interaction zone between air and fuel. In addition, it is seen in Fig.8 that the number of the smallest droplets at the outlet is smaller than that at the cavity. This may be because of the disappearance of some fragmented droplets along the x direction.

From Fig.9, when the evaporation is considered similar phenomena are also observed in the range of injection pressures of 0.5 to 4.0 MPa. That is, at either the cavity or the outlet the greatest number of the smallest droplets also appears at 0.5 and 4.0 MPa, respectively. However, compared with no evaporation, as shown in Figs. 8 and 9, the number of the smallest droplets for the injection pressure of 0.5 MPa reduces from 98.05% without evaporation to 97.65% with evaporation, while for the injection pressure of 4.0 MPa, the number is decreased from 92.81% to 90.94%. This reduction can be explained by the combined effects of shear interaction and evaporation. The shear

interaction causes big droplets to break up and simultaneously the evaporation promotes the fragmented droplets to become much smaller and subsequently disappear due to the increased evaporation area.

Based on the foregoing analysis, it is therefore inferred that the injection pressure has some effects on the number of the smallest kerosene droplet and hence on the injection breakup and the droplet atomization in cold supersonic flow. Note that the breakup condition of the droplet herein is based on the lower kerosene concentration. The lower concentration indicates the smaller size of the droplet [27]. This can basically be attributed to the fact that an increase in injection pressure results in an increase in total momentum of liquid jet from the orifice. The greater momentum generally contributes to the greater concentration of the smallest kerosene droplet. Under the effect of evaporation, a wider expansion area appears along the x direction, which is good to improve the mixture quality.

4. Comparison of Results with Published Data

As depicted above, the numerical predictions in this study are based on the real prototype of the 3D scramjet combustor used in Liu's experiment, but there are still no corresponding measurements available in literature. For numerical simulations verifying, the mixing characteristics between supersonic flow and kerosene injection for the different injection pressures have been qualitatively compared with the published data. These experimental evidences were obtained by such the approaches as high speed photography, high speed shadowgraph and particle image velocity (PIV) [28]. The comparisons are focused on penetration depth and span expansion area under identified working conditions. These conditions include an injection diameter of 1.0 mm, an injection angle of 90º, a supersonic-air velocity of Mach 2.0, and injection pressures ranging from 1.0 MPa to 4.0 MPa. The significant differences between the literature and this study are 1) the combustor structure (Figs. 1 and 10), and 2) the injection speed of the kerosene liquid. The injection speeds of the simulation and the measurement are 70 ms^{-1} and 63.2 ms^{-1}, respectively. The red rectangle in Fig.10 indicates an internal structure of the combustor different from that in this study.

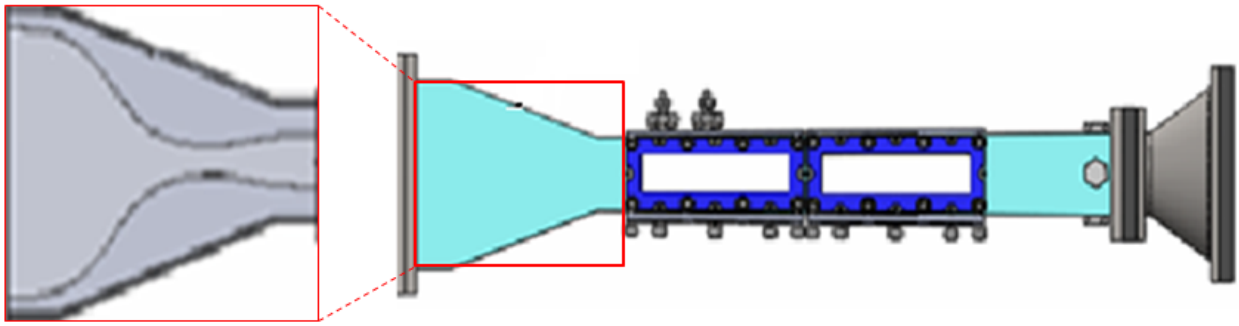

Fig.10. experimental setup of the scramjet combustor [28]

4.1. Penetration depth

Figure 11 shows original image photos of the penetration depth of the kerosene jet at four different injection pressures of 1.0, 2.0, 3.0 and 4.0 MPa. These experimental evidences were obtained by using high speed photography, high speed shadowgraph and particle image velocity (PIV), respectively. Figure 12 shows the comparison of the published experimental data with the numerical simulations in this study. As observed, the predicted patterns are qualitatively similar to those in the experiments: 1) the variation trend in penetration depth of the liquid jet is in good agreement with each other; 2) the penetration depth is increased with the injection pressure and 3) as the injection pressure is further increased the penetration depth is increased appreciably. For example, as the injection pressure is increased from 1.0 MPa to 2.0, 3.0, and 4.0 MPa the increased penetration depth is approximately 2 mm, 6 mm, and 8 mm, respectively. However, there is also the discrepancy in pressure value. That is, the penetration depths in this

study are much greater than those in [28]. This discrepancy may be explained as due to the different geometric structure of the combustor and due to the operation parameters, e.g. the injection speed. Generally, the greater injection speed of the kerosene liquid indicates the enhanced momentum and hence the higher penetration depth. Indeed, another comparison has also been implemented between Fig.5 and that in [29]. The qualitative agreement is also found that the penetration depth in [29] is also increased with the injection pressure.

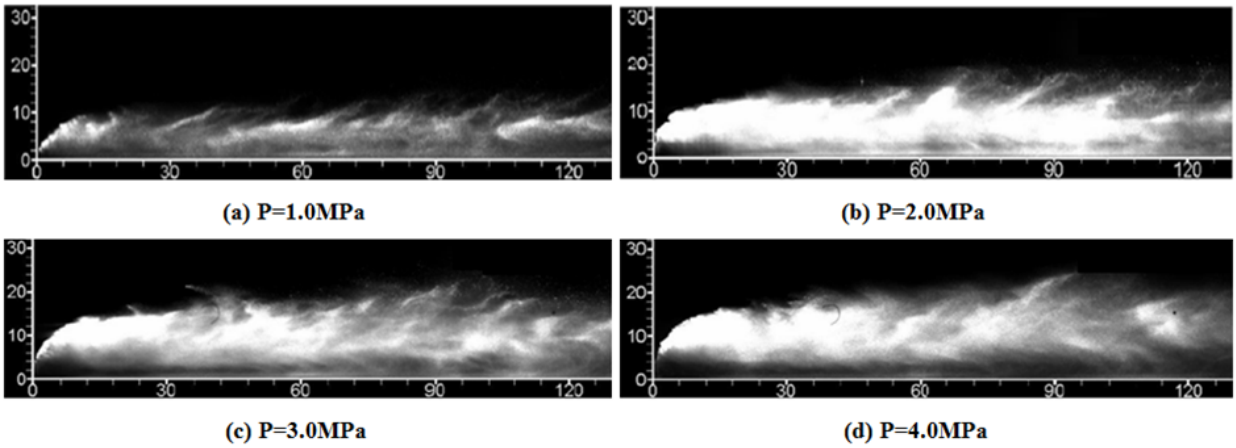

Fig.11. Original image photos of the penetration depth of the kerosene jet at four different injection pressures

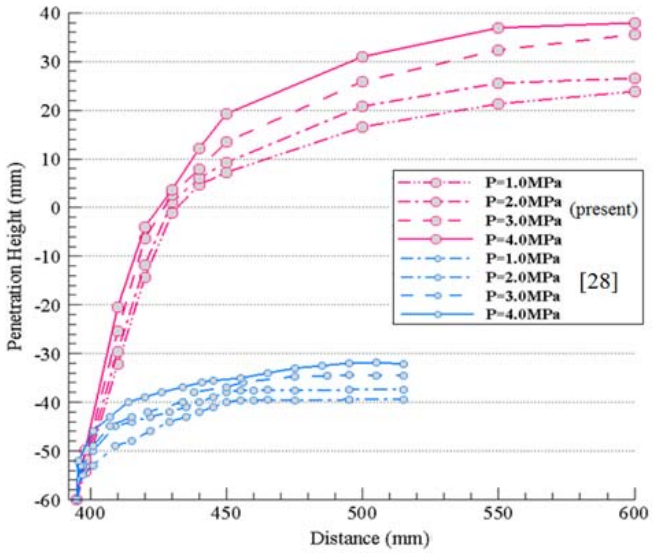

Fig.12.Comparison of calculated results with measurements in Fig.11

4.2. Span expansion area

Figure 13 shows the span expansion areas of the kerosene jet at four different injection pressures of 1.0, 2.0, 3.0, and 4.0 MPa in [28]. It should be noted that these experimental evidences are measured at the position of 15mm vertically away from the orifice of the combustor and that the used experimental approach and equipment are identified with those in Fig.11. The measured span expansion areas, including span angles and breadths, have been compared against the numerical simulations in this study, as shown in Fig.14. It is observed that the measured variation trends in either span angle or expansion breadth are good qualitative agreement with the calculated results. In detail, both the span angle and breadth are increased with the injection pressure. But, the difference in value of the span expansion area still exists between CFD predictions and experimental measurements. The span expansion area is larger than that in [28].This may be also attributed to the different geometric structure of the combustor and

operation conditions, i.e. the injection speed. The larger injection speed of the kerosene liquid leads to the greater momentum, which, in turn, contributes to the more injection mass and hence enlarges the span expansion area.

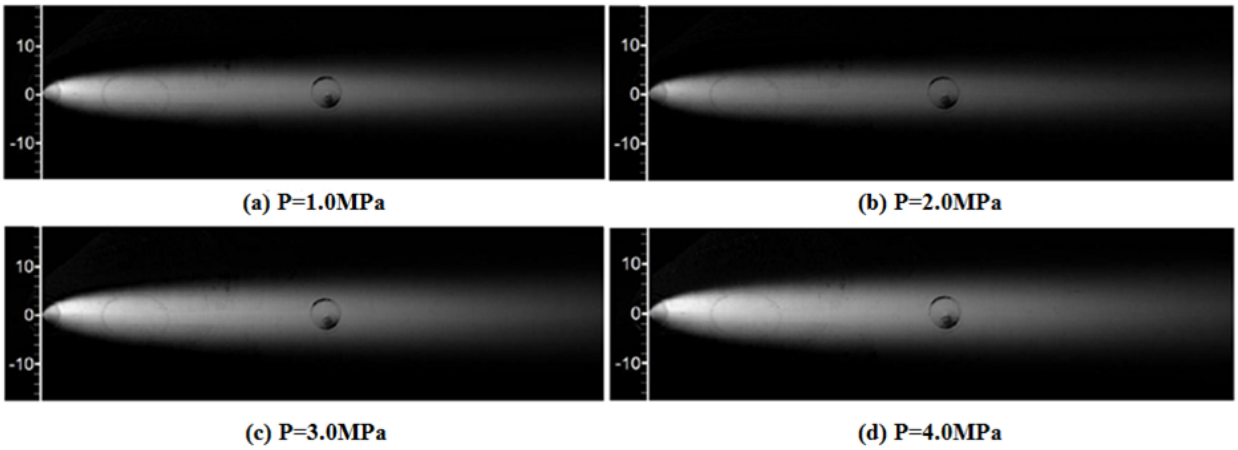

Fig.13. Measured span expansion area of liquid jet under the different injection pressures [28]

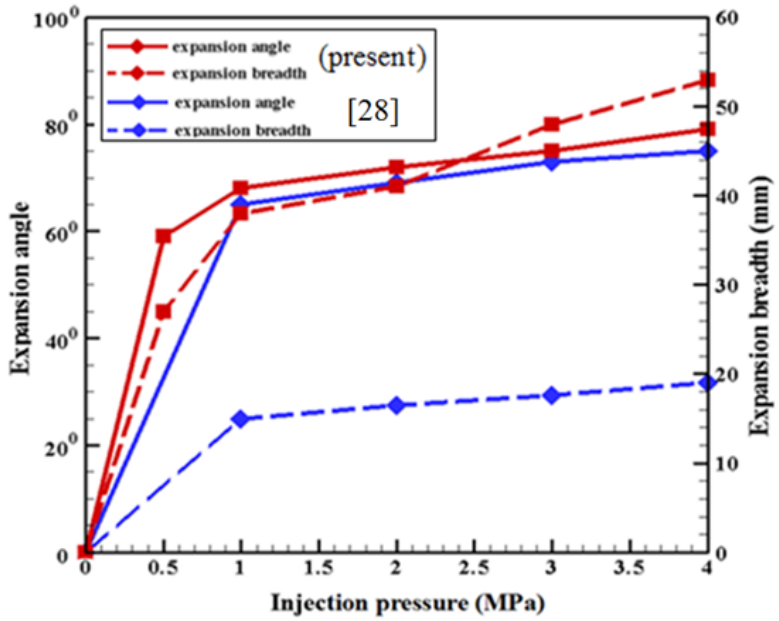

Fig.14. Comparison of the calculated span expansion areas with the measurements under the different injection pressures

Although there are some discrepancies in magnitude, the foregoing results validate that the predicted effects of the injection pressures on mixing in the cold supersonic flow are in qualitative agreement with those in literature and that a combination of CLSVOF and improved K-H & R-T models can offer great potential for the in-depth study of fundamental mechanisms of the liquid jet in the high speed crossflow.

5. Conclusions

A numerical investigation has been implemented to assess the effects of the injection pressure on the mixing in the cold supersonic combustor with kerosene fuel. The mixing characteristics in the range of injection pressure of 0.5 to 4.0 MPa are investigated, respectively. Evaluation are performed primarily with respect to four aspects for fuel/air mixing, namely, penetration depth, span expansion area, angle of shock wave, and sauter mean diameter distribution

with/without the evaporation considered.

This work has demonstrated that varying injection pressure has the effects on the mixing between kerosene and air. In detail, the penetration depth, span expansion area and shock wave angle of the kerosene droplets are increased with the injection pressure, respectively and that the greatest number of the smallest kerosene droplets appears either at the orifice for 0.5 MPa or at the outlet for 4.0 MPa no matter whether the evaporation is considered. However, it should be noted that the penetration depth increases appreciably as the injection pressure is further increased. Hence, it is concluded that even if the injection pressure can provide some increase in the penetration depth, its effect in the practical applications is shown to be less pronounced than anticipated. The numerical simulations in this study have been compared against the reported experimental measurements with good qualitative agreement although the difference in value exits.

Overall important insights have been gained into the physical behavior and key factors for fuel injection in the cold supersonic combustor at the five different injection pressures, adding to the knowledgebase usefully applicable to the design of high performance fuel injection systems for scramjets. However, the current results suggest further investigations. The effects of the structural characteristics, e.g. the geometric parameters and shapes of the cavity on the mixing between fuel and air need to be addressed in the forthcoming study.

Acknowledgments

The authors acknowledge financial support for this work from the National Natural Science Foundation of China (Grant No. 11272309, 51575003), Anhui Provincial Natural Science Foundation (Grant No.1508085ME71) and Key Project of Anhui Education Committee (Grant No. KJ2015A031). The authors also thank the reviewers for their valuable input.

References

[1] C. Zhang, Q.Yang, J. Chang, J. Tang, W.Bao, Nonlinear characteristics and detection of combustion modes for a hydrocarbon fueled scramjet, Acta Astronautica. 110 (2015) 89-98.

[2] Hideaki Ogawa, Effects of injection angle and pressure on mixing performance of fuel injection via various geometries for upstream-fuel-injected scramjets, Acta Astronautica. 128 (2016) 485-498.

[3] V.P.Karpov, G.G. Politenkova, E.S. Severin, Turbulent burning of alcohol, Combust, Explos., Shockwaves 22(4)(1986)12–14.

[4] W. Huang, L. Ma, M. Pourkashanian, D.B. Ingham, S.B. Luo, Z.G. Wang, Parametric effects in a scramjet engine on the interaction between the air stream and the injection, Proceedings of the Institution of Mechanical Engineers, Part G:Journal of Aerospace Engineering. 226 (3) (2012) 294–309.

[5] T. Mai, Y. Sakimitsu, H. Nakamura, Y. Ogami, T. Kudo, H. Kobayashi, Effect of the incident shock wave interacting with transversal jet flow on the mixing and combustion, Proceedings Combustion Institute.33(2) (2011) 2335–2342.

[6] E. Erdem, K. Kontis, Numerical and experimental investigation of transverse injection flows, Shock Waves 20 (2)(2010) 103–118.

[7] A. Abdelhafez, A.K. Gupta, R. Balar, K.H. Yu, Evaluation of oblique and traverse fuel injection in a supersonic combustor, in: 43rd AIAA/ASME/SAE/ASEE Joint Propulsion Conference & Exhibit, OH, Cincinnati, AIAA Paper (2007) 2007–5026.

[8] W. Huang, Z.G. Wang, L. Yan, W.D. Liu, Numerical validation and parametric investigation on the cold flow field of a typical cavity-based scramjet combustor, Acta Astronautica. 80(2012) 132–140.

[9] J.Hu, J.Chang, W.Bao, Q.Yang, J.Wen, Experimental study of a flush wall scramjet combustor equipped with strut/wall fuel injection, Acta Astronautica. 104(2014) 84-90.

[10] Wei-Lai Liu, Laser dropsizing of kerosene injected into a supersonic airstream, the project supported by the National Natural Science Foundation of China (Grant No.11272309)

[11] Lin Zhu, Shuang-Shuang Peng, Yin-Yin Qi, Xi Cheng, Wen-Feng Zhang, Liang-Yuan Xu, De-Quan Zhu, An improved horizontally reversible plow design based on virtual assembly semantics and constraint, Journal of Mechanical Science and Technology. 30(2016) 257-266.

[12] Lawson,S.J.,Barakos,G.N., Review of numerical simulations for high-speed, turbulent cavity flows. Prog. Aerosp. Sci. 47(2011)186-216.

[13] Ukai, T., Zare-Behtash, H., Erdem, E., Lo, K.H., Kontis, K., Effectiveness of jet location on mixing characteristics inside a cavity in supersonic flow, Exp.Therm. Fluid Sci. 54(2014)59-67.

[14] Olsson E, Kreiss G. A conservative level set for two phase flow, Journal of computational physics. 210(2005) 225-246.

[15] Nickolay N.Smirnov, Valeriy F. Nikitin, Vladislav R. Dushin, Yurii G. Filippov, Valentina A. Nerchenko, Javad Khadem. Combustion onset in non-uniform dispersed mixtures, Acta Astronautica, 155(2015) 94-101.

[16] V.B.Betelin, V.F.Nikitin, A.G.Kushnirenko, V.A. Nerchenko, N.N.Smirnov. Spray injection and ignition in a heated chamber modeling, WSEAS Trans Fluid Mech. 1790-50876 3(2011)147-159.

[17] V.B.Betelin, N.N.Smirnov, V.F. Nikitin, V.R. Dushin, A.G.Kushnirenko,V. A. Nerchenko. Evaporation and ignition of droplets in combustion chambers modeling and simulation, Acta Astronautica, 70(2012) 23-35.

[18] F.R.Menter, M.Kuntz, R.Langtry. Ten years of experience with the SST turbulence model, Heat and Mass Transfer, 4, Begell House Inc 2003, 625-632.

[19] Wei Huang, Liang Jin, Li Yan, Jian-guo Tan, Influence of jet-to-crossflow pressure ratio on nonreacting and reacting processes in a scramjet combustor with backward-facing steps, Int. J. Hydrog. Energy, 2014 (36) 39-45.

[20] W. Huang, W.D. Liu, S.B. Li, Z.X. Xia, J. Liu, Z.G. Wang, Influences of the turbulence model and the slot width on the transverse slot injection flow field in supersonic flows, Acta Astronautica 73(2012) 1-9.

[21] Driscoll R, St George A, Gutmark E, Numerical investigation of injection within an axisymmetric rotating detonation engine, International Journal of Hydrogen Energy, 41(2016) 2052-2063.

[22] A. I. Glagolev, A, I. Zubkov, and Yu. A. Panov, supersonic flow past a gas let obstacle emerging from a plate, Fluid dynamic, 2(3) (1967)97–102.

[23] Jing Liu. Numerical and experimental investigation of fuel spray in supersonic cross flow. PhD dissertation, Beihang University, Beijing, China, 2010.

[24] C.Ortiz, D.D.Joseph, and G.S.Beavers. Acceleration of a liquid drop suddenly exposed to a high-speed airstream, International Journal of Multiphase Flow, 30(2004) 217-224.

[25] Driscoll R, St George A, Gutmark E, Numerical investigation of injection within an axisymmetric rotating detonation engine, International Journal of Hydrogen Energy, 41(2016) 2052–2063.

[26] V.R. Dushin, A.V. Kulchitskiy, V.A. Nerchenko, V.F. Nikitin, E.S. Osadchaya, Yu.G. Phylippov, N.N. Smirnov, Mathematical simulation for non-equilibrium droplet evaporation, Acta Astro- nautica 63 (2008) 1360–1371.

[27] Joseph D.D., Belanger J., Beavers G.S., Breakup of a liquid drop suddenly exposed to a high-speed airstream. International Journal of Multiphase Flow, 25 (1999) 1263-1303.

[28] Chun Li, Injection Structural characteristics of transverse liquid jet in supersonic crossflow, Master thesis, National University of Defense Technology, P.R.China, 2013.

[29] A. I. Glagolev, A, I. Zubkov, and Yu. A. Panov, supersonic flow past a gas let obstacle emerging from a plate, Fluid dynamic. 8(2) (1968) 99–103.